PHYSICAL REVIEW C VOLUME 46, NUMBER 5 NOVEMBER 1992

Neutron–charged-particle correlations in the 3.8 MeV per nucleon $^{16}O+^{12}C$ and 13.4 MeV per nucleon $^{16}O+^{27}Al$ reactions

R. A. Kryger,* J. J. Kolata, W. Chung, S. Dixit, R. J. Tighe, and J. J. Vega†
Department of Physics, University of Notre Dame, Notre Dame, Indiana 46556

P. A. DeYoung, C. Copi, and J. Sarafa
Physics Department, Hope College, Holland, Michigan 49423

G. P. Gilfoyle and S. K. Sigworth
Physics Department, University of Richmond, Richmond, Virginia 23173

(Received 16 April 1992)

Neutron–light-charged-particle (LCP) and LCP-LCP correlation functions were measured for the 215 MeV $^{16}O+^{27}Al$ reaction, together with the neutron-proton correlation function for the $^{16}O+^{12}C$ reaction at $E_{\text{lab}}=60.5$ MeV. The *np* and *pp* correlation data are compared with the predictions of the Koonin model and a semiclassical evaporation model. Both models provide an excellent fit to the *np* data, while the *pp* data are not reproduced as well. Production yields of singlet deuterons, ground state ^{5}He and ^{5}Li, and ^{6}Li nuclei in the 2.186 MeV state were obtained from the coincidence data, and a nuclear temperature of $T=2.0^{+0.8}_{-0.6}$ MeV for the $^{16}O+^{27}Al$ compound system was determined from the ratio of singlet to ground state deuteron emission, after corrections for sequential emission and noncompound deuteron production. This temperature value is well below the Fermi gas model estimate, and a similar result is observed for the $^{16}O+^{12}C$ compound system.

PACS number(s): 25.70.−z, 25.70.Gh, 25.70.Pq

I. INTRODUCTION

Two-particle correlations between coincident light particles detected at small relative angles can result from a variety of sources including final-state Coulomb and nuclear interactions, quantum statistics, and the emission of particle-unstable composite nuclei [1–6]. The effect of these interactions on the measured correlation function depends upon the size and lifetime of the emitting source, the emission dynamics of the coincident particles, and the nature of the two-particle forces. These various effects have been the subject of intense investigation; many two-particle correlation experiments have been performed for a variety of reactions and over a wide range of energies [1]. At present, the preponderance of two-particle correlation data involves coincidences between light charged particles LCP-LCP, although a few neutron-neutron (*nn*) results have been published [7–9]. We report on two *n*-LCP correlation experiments for the 13.4 MeV per nucleon $^{16}O+^{27}Al$ reaction and the 3.4 MeV per nucleon $^{16}O+^{12}C$ reaction. The principal motivation behind this work was twofold. First, we wanted to measure neutron-proton (*np*) and proton-proton (*pp*) correlation functions for the same reaction and to compare model predictions for these two-particle systems with the data. The *np* system provides an excellent test for correlation models since the low-relative-momentum correlation data are free of correlations due to wave-function antisymmetrization or effects due to the Coulomb interaction between the neutron and proton. Second, small-angle *np* correlation data allow a determination of the singlet-deuteron (d^*) emission probability relative to ground-state deuterons. From this information the nuclear temperature can be determined using the "deuteron thermometer" [10], by comparing the relative emission probability of the two states. Similar temperature measurements have been accomplished by small-angle correlation experiments as well as other methods [11–23]. Many of these experiments have found surprisingly low nuclear temperatures compared with the values expected from the Fermi-gas model or deduced from kinetic-energy spectra of light particles. The deuteron provides an interesting temperature probe because of its low mass and the fact that it only has one excited state. The present data comprise the first measured correlation functions for neutron-proton, neutron-deuteron (*nd*), and neutron–alpha-particle (*nα*) systems. Preliminary results from this work were published in Ref. [22].

Sections II and III of this manuscript describe the experimental method and the computation of the relative-momentum correlation functions. In Sec. IV model predictions for the *np* and *pp* correlation functions are compared with the data. The determination of the singlet-deuteron cross section (as well as that of several other particle-unstable fragments) is discussed in Sec. V, and the results from the deuteron thermometer are presented

---

*Present address: NSCL/Cyclotron Laboratory, Michigan State University, East Lansing, MI 48824-1321.

†Present address: Instituto Nacional de Investigaciones Nucleares, Mexico.

in Sec. VI. Finally, the results are summarized and our conclusions are presented in Sec. VII.

II. EXPERIMENTAL METHOD

The first experiment was completed at the Argonne National Laboratory ATLAS heavy-ion accelerator using a 215-MeV pulsed ^{16}O beam incident on a 800-μg/cm^2 Al target. Coincident particles were detected in two arrays of detectors centered at ±45° with respect to the incident beam. Each detector array consisted of three NaI(Tl) LCP detectors in the horizontal plane, combined with four NE-213 liquid scintillator neutron detectors. The neutron detectors were placed behind the charged-particle detectors, and slightly above and below the horizontal plane, to minimize the relative angle between neighboring detectors and to avoid shielding of the neutron detectors by the NaI(Tl) detector housings. In this configuration there are eight pairs of n-LCP detectors with center-to-center opening angles of 3.1°, eight pairs with an opening angle of 3.2°, and eight additional pairs with opening angle of 5.4°. The 24 combinations of across-beam pairs of n-LCP detectors had opening angles near 90°. The upper two plots in Fig. 1 show projections of the solid angle of the individual detectors in the polar (Θ) and azimuthal (Φ) angle plane with respect to the incident beam.

The six charged-particle detectors consisted of 5.0-cm-diam by 3.8-cm-long cylindrical NaI(Tl) crystals coupled to photomultiplier tubes and covered with protective 6-mg/cm^2 Havar [24] foils. Each detector was placed 1.3 m from the target and collimated to a diameter of 3.8 cm, thus subtending a solid angle of 0.7 msr. Charged-particle identification was accomplished off line using the energy, time-of-flight (TOF), and pulse-shape information by the method described in Refs. [25] and [26], leading to the unambiguous identification of protons, deuterons, tritons, ^{3}He, and alpha particles. Energy calibrations for $Z=1$ (protons and deuterons) and $Z=2$ (alpha particles) were obtained via the kinematics of ^{6}Li breakup and the ^{12}C(^{16}O,α) reaction at several beam energies. We made use of identical proton and deuteron energy calibrations (after correcting for energy loss in the Havar foil) following the detailed study of NaI(Tl) detector properties by Maguire *et al.* [27], who found that the energy versus light output is nearly the same for these particle species, with less than 5% variation for energies between 10 and 50 MeV. The relative energy resolution for $Z=1$ particles was estimated to be $\leq 6\%$ at an energy of 24 MeV, based upon the full width at half maximum (FWHM) of the H-knockout peak (arising from H contamination in the target) observed in the singles proton spectra. Low-energy thresholds of 2.5, 2.7, and 6.6 MeV for protons, deuterons, and alpha particles, respectively, were imposed by energy loss in the protective Havar foils used in the detectors.

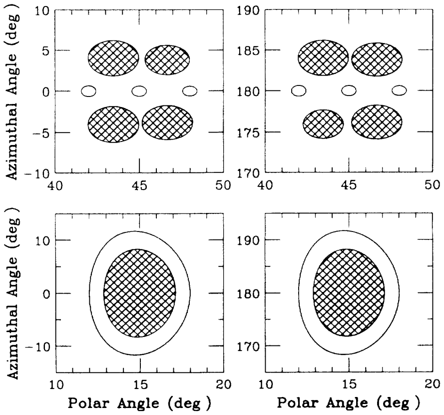

FIG. 1. Angular coverage of the neutron detectors (crosshatched regions) and charged particle detectors (unshaded regions) in the ^{16}O$+^{27}$Al experiment (upper two plots) and the ^{16}O$+^{12}$C experiment (lower two plots).

The eight neutron detectors consisted of cylindrical NE-213 liquid scintillator cells coupled to fast-timing photomultiplier tubes. Six of the detectors had scintillator cells of dimensions 12.5 cm diam by 7.5 cm long, and two had dimensions of 10.2 cm diam by 7.5 cm long. Each detector was placed 2.4 m from the target (average solid angle of 2.0 msr) and viewed the target through a 0.3-cm-thick Al vacuum chamber wall, 1.2 m of air, and a 0.13-cm-thick Pb shield used to reduce the flux of target γ rays. Time-of-flight and pulse-shape signals were recorded for each detected particle. The neutron energy was determined from the TOF, measured relative to the 260-ps FWHM ^{16}O beam pulses. Total neutron TOF resolution was between 0.7 and 1.0 ns (for the various detectors), leading to a relative energy resolution of 3% for 5-MeV neutrons. Contaminant γ-ray events were removed off line by making use of TOF gates and standard pulse-shape discrimination techniques [28]. A further requirement that neutron events deposit at least 2 MeV in the detector ensured excellent n/γ-ray separation by pulse shape and eliminated the possibility of confusion between low-energy neutrons from one beam burst and high-energy neutrons from the next beam burst on target (consecutive beam pulses were separated by 240 ns). Neutron shadowbars, consisting of 6.7-cm-diam by 25-cm-long brass cylinders, were placed halfway between the detector and target to allow estimation of coincidence event rates due to scattered neutrons. Each detector was shielded for approximately $\frac{1}{3}$ of the total beam time on target, and the scattered neutron background was removed off line as described in the next section.

Coincident events were recorded between particles from the same or consecutive beam burst on target. The latter provided a simultaneous measurement of the random coincidence background, which was also subtracted from the coincidence data.

The incident beam passing through the target was collected in a beam dump approximately 4 m downstream, consisting of a Faraday cup shielded by concrete, Pb, and borated plastic to minimize the effects of background radiation on the neutron detectors. Additional shielding was placed around the beam-line collimators upstream from the target and around all of the neutron detectors. It was not necessary to eliminate completely background radiation from these sources, however, because their effects on the coincidence data were measured as described above.

The second experiment was performed at the University of Notre Dame Nuclear Structure Laboratory using the FN Tandem accelerator to produce a 60.5-MeV ^{16}O beam which was incident on a 200-μg/cm^2 C target. In this case, protons were detected in two three-element Si detector telescopes placed at ±15° with respect to the beam ($\Theta = 15°$, $\Phi = 0°$ and 180°), and coincident neutrons were detected in two detectors centered directly behind the proton telescopes. Figure 1 shows the angular coverage of the detectors in this experiment. In this configuration the opening angle between the centers of the nearest neutron and proton detectors was 0°.

The proton telescopes consisted of two thin transmission-mounted Si surface barrier detectors ($\Delta E_1 = 50$ μm and $\Delta E_2 = 300$ μm thick) and a thicker transmission-mounted Si(Li) detector ($E = 5000$ μm thick). Each telescope was collimated to a 6 mm diam and placed at a distance of 5.5 cm from the target. A 30-mg/cm^2 Ta foil was inserted in front of the ΔE_1 detector to stop scattered heavy ions ($Z \geq 3$). The detectors were energy calibrated using the H(^{16}O,p) reaction on contamination H in the target, for various ^{16}O beam energies. The relative proton energy resolution is estimated to be 5% FWHM for 12-MeV protons, based upon the width of the proton peak in the energy calibration runs. Only protons penetrating into the 300-μm detectors were accepted, allowing particle identification to be accomplished by ΔE_1-vs-ΔE_2 energy-loss comparisons. This latter condition resulted in a 2.2-MeV proton energy threshold.

The neutron detectors consisted of 12.5-cm-diam by 7.5-cm-long cylindrical cell NE-213 liquid scintillator detectors, similar to those previously described. These detectors were placed 1.75 m from the target and viewed the target through a 1-mm-thick stainless-steel vacuum chamber wall, about 1.6 m of air, and a 2-mm-thick Pb γ-ray suppression shield. As before, neutron energy was determined by TOF, but in this case the TOF was measured relative to the detection time of the coincident proton since the beam was not pulsed. We achieved an energy resolution of 5% (FWHM) for 5-MeV neutrons. TOF and pulse-shape discrimination were also used as before to screen out the contaminant γ rays. Clean neutron/γ-ray separation required a 1.0-MeV software threshold on the energy deposited in the neutron detectors. No shadowbar measurements were made in this experiment for the reasons discussed in the next section.

III. CORRELATION FUNCTIONS

The correlation function for a given pair of coincident particles, in terms of the magnitude of the relative momentum vector **q** of the particles, is given by

$$C(q) = A(q)/B(q) , \tag{1}$$

where $A(q)$ is the relative momentum spectrum of the coincidence data corrected for background sources of coincidence events and $B(q)$ is a reference spectrum which represents the coincidence data as it would have been measured in the absence of the correlations of interest. In our case the correlations of interest include mutual interactions between the detected particles (such as the Coulomb or nuclear forces) and the effects of the decay of composite particles. However, experimentally induced correlations such as those that might be imposed by the detector thresholds, efficiencies, etc., are not of interest and should ideally be represented in the reference spectrum $B(q)$ exactly as they are in $A(q)$ so that their effects cancel out in the evaluation of the correlation function. The uncorrelated coincidence data, from which $B(q)$ is ascertained, cannot be measured directly and were approximated by event mixing [29]. In this procedure one constructs a set of pseudoevents from the measured coincidence data by interchanging the momentum vector of one of the particles between time-ordered pairs of coincidence events. Two-particle correlations, which manifest themselves in the difference between the momenta of a pair of coincident particles, are strongly suppressed. On the other hand, the individual momentum distributions of each particle type are preserved in the mixed data. This technique is similar to the other common method of constructing the reference spectrum, taking a normalized product of the single-particle momentum distributions, but in this latter method the singles events may not all arise from the same types of reactions as the coincidence data [30]. Our event-mixing procedure only utilized events for particles detected in the same pairs of detectors and originating under the same conditions of identical or consecutive beam bursts and shadowed or unshadowed neutron detectors, thereby preserving all of the detector threshold and efficiency effects in the event-mixed data that were present in the measured data.

The n-LCP relative momentum spectrum $A(q)$ for the ^{16}O$+^{27}$Al reaction was corrected for the scattered neutron and random coincidence events before the ratio $C(q)$ was evaluated. The background-corrected data are defined by

$$A(q) = Y_{\mathrm{raw}}(q) - Y_{\mathrm{shad}}(q) - \tfrac{1}{2} Y_{\mathrm{ran}}(q) , \tag{2}$$

where $Y_{\mathrm{raw}}(q)$ is the relative-momentum spectrum generated from all coincidence events originating in the same beam burst on target and without the neutron detector shadowed, $Y_{\mathrm{shad}}(q)$ is the spectrum generated from coincidence events in which each particle originated from the same beam burst on target and the neutron detector was shadowed [normalized relative to $Y_{\mathrm{raw}}(q)$ by the ratio of incident beam on target with the neutron detectors unshadowed to beam on target with the detectors shadowed], and $Y_{\mathrm{ran}}(q)$ is the relative-momentum spectrum corresponding to events in which the particles originated from consecutive beam bursts with an unshadowed neutron detector minus the spectrum corresponding to events in which the particles originated from consecutive beam bursts with a shadowed neutron detector (these latter two spectra are normalized by the ratio of incident beam on target under each condition before subtraction). With these definitions, $Y_{\mathrm{shad}}(q)$ corresponds to the spectrum of background events in which the neutron scattered between the target and detector, including random coincidences between scattered neutrons and charged particles. $Y_{\rm ran}(q)$ represents the relative-momentum spectrum for random coincidence events involving unscattered neutrons. The factor of $\frac{1}{2}$ in Eq. (2) is present because the random coincidence rate due to particles produced in two consecutive beam bursts (with either particle originating in either beam burst) is twice the rate due to particles produced in the same beam burst. The identical background subtraction technique was applied to the event-mixed data to form $B(q)$. The shadowbar background, as defined above, constituted 32% of the coincident *np* events, and the random background accounted for an additional 8%. The other *n*-LCP combinations had similar background rates. The relatively high shadowbar background probably resulted from neutron scattering from the abundance of material (vacuum chamber walls, pumps, etc.) that was present in the vicinity of the target and detectors. Equation (2) was also used to define $A(q)$ and $B(q)$ for the LCP-LCP coincidence data, with the scattered particle terms set to zero. The random background contribution for the *pp* coincidence data constituted 23% of the total coincident events.

The relative momentum spectra $A(q)$ and $B(q)$ were not background corrected for the lower-energy ^{16}O+^{12}C reaction data. This was done for two reasons. First, the background levels were significantly lower in this case than for the ^{16}O+^{27}Al reaction. The random background was 10% of the coincidence *np* data, based upon the number of neutrons observed with an uncorrelated TOF relative to the coincident proton. The scattered neutron background was not measured, but is estimated to be approximately 12% of the total *np* events based upon a test run for the ^{16}O+^{12}C experiment at 56 MeV. Second, the *np* data for this lower-energy reaction proved to be essentially free of two-particle correlations, and so it was not necessary to make a quantitative analysis of the correlation data.

The *n*-LCP correlation functions measured in the current set of experiments are shown in Figs. 2 and 3, including neutron-proton, neutron-deuteron, and neutron–alpha-particle combinations. (The number of *n*-triton or *n*-^{3}He events measured in the ^{16}O+^{27}Al reaction was too low to allow correlation functions to be computed.) The data points at low *q*, corresponding to coincidence events measured in pairs of detectors with small opening angles (on the same side of the beam), are shown with solid circles. The large-opening-angle data (not shown for the 60.5-MeV *np* data) are displayed with open square symbols. These latter data were relatively free of two-particle correlations for each of the *n*-LCP combinations, and the correlation functions are flat and average to unity as indicated by the solid lines in Fig. 2. The small-opening-angle data, on the other hand, show considerable structure. Both the *np* and *nα* correlation functions for the 215-MeV ^{16}O+^{27}Al reaction show peaks in the correlation functions, near 0 and 37 MeV/*c*, respectively. These peaks are due to the particle-unbound singlet-deuteron (d^*) state and the ^{5}He ground state. Both peaks rest upon a flat background, in the low-*q* region of the correlation function, which has an average value that is considerably less than unity, thus causing a disjunction in the magnitude of the correlation ratio between the small- and large-opening-angle data. This disjunction results from the conservation of the number of events in the event-mixing procedure which produced the reference spectrum $B(q)$. Relative to $A(q)$, the number of events in the reference spectrum will be overestimated (underestimated) if the measured coincidence data contain positive (negative) correlations, since a correlation represents an excess (or deficit) of events in $A(q)$ that should not be present in $B(q)$. Thus, while the correlation ratio for the large-opening-angle data (which are free of correlations) averages to unity, the small-angle *np* and *nα* correlation functions fall below unity because of an

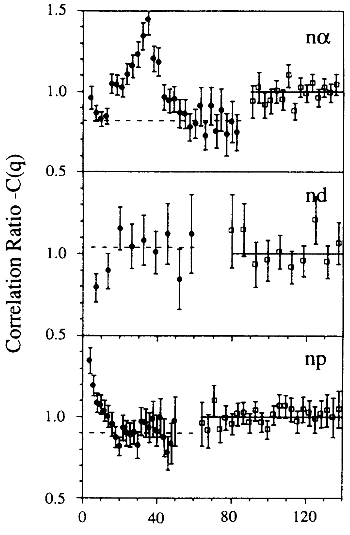

FIG. 2. *nα*, *nd*, and *np* correlation functions from the ^{16}O+^{27}Al reaction as a function of relative momentum. The solid circles denote the small-opening-angle coincidence data, and the open square symbols denote the large-opening-angle data. The solid and dashed lines are explained in the text.

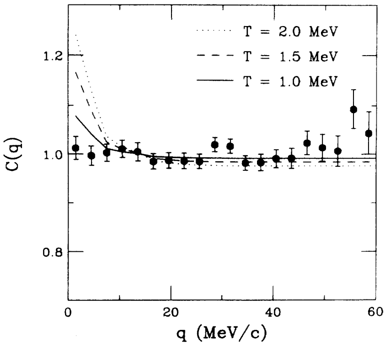

FIG. 3. Small-opening-angle *np* correlation function measured for the ^{16}O+^{12}C reaction as a function of relative momentum. The solid, dashed, and dotted lines are the results of calculations discussed in Sec. VI.

overestimation of the number of events in $B(q)$. The background levels of the correlation functions in the low-q region were determined in these two cases by averaging the correlation data away from the peaks. These averages were 0.90 ± 0.03 and 0.82 ± 0.03 for the *np* and *nα* cases, respectively, and are indicated by the dashed lines in Fig. 2.

The 60.5-MeV $^{16}O+^{12}C$ *np* correlation function in Fig. 3 shows no clear evidence for the positive singlet-deuteron correlation and is in fact consistent with unity over the whole q range. A weaker d^* signal was expected for the 60.5-MeV $^{16}O+^{12}C$ reaction (relative to the 215-MeV $^{16}O+^{27}Al$ reaction) since a lower reaction energy usually results in the emission of fewer composite particles. However, the complete lack of a positive correlation was quite unexpected. A further discussion of these data (and the curves shown in Fig. 3) is found in Sec. VI.

A low-q anticorrelation was observed in the $^{16}O+^{27}Al$ reaction *nd* correlation function. The average flat background, shown by the dashed line in Fig. 2, was determined to be 1.04 ± 0.07 by averaging the small-opening-angle correlation data away from the dip at very low q. Although there is considerable statistical uncertainty associated with these data, there are at least two possible physical sources for a real anticorrelation: the coalescence of low-q *nd* pairs into tritons, which would not be observed as *nd* events, or a repulsive component of the *nd* nuclear force which scatters low-q *nd* pairs. (Unlike the case for similar anticorrelations observed at low q in LCP-LCP correlation data, the source cannot be the Coulomb interaction since the neutron is uncharged.) In fact, the $J=\frac{3}{2}$ s-wave *nd* interaction is strongly repulsive [31] because of Pauli repulsion between the two neutrons.

The charged-particle correlation functions are shown in Figs. 4 and 5. The results were qualitatively similar to analogous correlation functions measured in the $^{16}O+^{27}Al$ reaction [32,33] and in other reactions [34]. As in Fig. 2, the small-opening-angle data are displayed with solid circles and the large-opening-angle data with open squares. The *αα* correlation function shows a large peak at $q\approx20$ MeV/c, as a result of the breakup of the α-unbound ^8Be ground state, superimposed upon a sloping background that results from the Coulomb repulsion between alpha particles, which suppresses *αα* pairs at small relative momentum. The overall normalization of the small-opening-angle correlation ratio is shifted below unity, as in the *np* and *nα* cases, as a result of the presence of the ^8Be peak, leading to the discontinuity in the correlation function at $q\approx180$ MeV/c. The *dd* and *pp* correlation functions both display anticorrelations at low q because of Coulomb repulsion. In the *pp* system, the Pauli exclusion principle may also suppress low-q pairs of protons, possibly enhancing the anticorrelation. The *pp* correlation function also shows a possible indication of a peak in the range $10\leq q\leq30$ MeV/c, which may result from the unbound ^2He state. A strong peak due to this virtual state has been observed in *pp* correlation data at higher energies [35]. The *dα* correlation function is dominated by a peak due to the decay of the first excited state of ^6Li ($^6Li^*$, $E_x=2.186$ MeV, $J^\pi=\frac{3}{2}^-$), with a sloped background at low q due to Coulomb repulsion. The *pα* correlation function, on the other hand, shows two peaks. The broad peak at $q\approx60$ MeV/c is due to the particle-unstable ^5Li ground state ($J^\pi=\frac{3}{2}^-$, $\Gamma\approx1.5$ MeV). The narrow peak at $q\approx10$ MeV/c was identified by Pochodzalla *et al.* [36] as due to the three-body breakup of ^9B into two alpha particles and a proton. Finally, the *pd* correlation function shows the expected Coulomb anticorrelation. The disjunction in the magnitude of the average correlation ratio between the small- and large-opening-angle data is again a manifestation of the normalization shift due to event mixing.

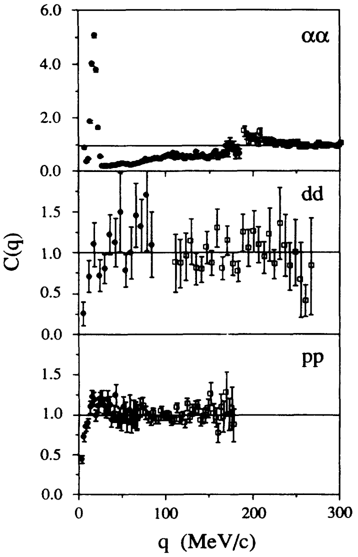

FIG. 4. *αα*, *dd*, and *pp* correlation functions from the $^{16}O+^{27}Al$ reaction.

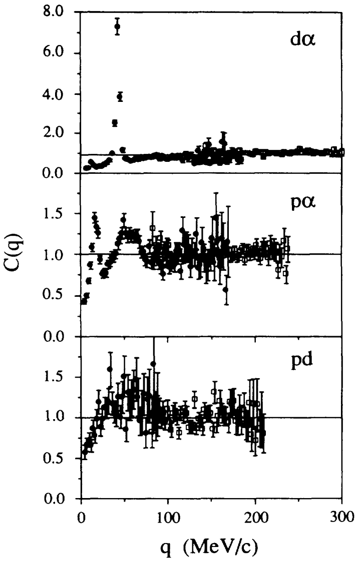

FIG. 5. *dα*, *pα*, and *pd* correlation functions from the $^{16}O+^{27}Al$ reaction.

IV. MODEL ANALYSIS

Ideally, a model description of the two-particle correlation function should account for all possible sources of correlations including two-particle interactions (Coulomb or nuclear), quantum effects such as Pauli repulsion for identical fermions, correlations that arise due to the interaction of the two particles with the source [37,38], and correlations induced by the experimental technique (such as detector placement or energy cuts). In practice, approximations are made in treating the various sources of correlations, and different models have been refined to study different effects. We have made use of two distinct models in this study. The first is a semiclassical Monte Carlo simulation of the evaporation of coincident particles from the surface of a compound nucleus [39–41]. Classical interactions between the emitted particles, such as the Coulomb interaction, are easily included in this type of model, as is the emission of composite particles which decay in flight. On the other hand, resonant final-state nuclear interactions and other quantum phenomena including wave-function (anti)symmetrization are difficult to include. The second model we used is the familiar Koonin model [1,3], a quantum treatment of the two-particle correlations. In this model the two-particle wave function is constructed (including Coulomb, nuclear, and quantum-statistical effects) and the correlation function is computed from this wave function. This model, however, does not treat interactions between the emitted particles and the residual compound system. Our initial effort has been directed toward evaluating these two models for the *np* system and then comparing with the *pp* system to gain further insight. The other *n*-LCP and LCP-LCP systems will be treated in more detail in a future publication.

The Monte Carlo evaporation model calculations were performed using the computer code MENEKA [39]. The evaporation of light particles from the compound system is modeled by the stepwise emission of particles from a progressively cooler residual nucleus. For each particle type, the probability of emission, P_i, the emission time distribution $t_i = \exp(-t/\tau_i)$, and the emission energy distribution, given by

$$Y_i(E) \propto (E - V_i)^2 \exp(-E/T_i) , \tag{3}$$

are determined from a statistical model decay code as a function of the particle's position i in the decay chain. MENEKA then generates two-particle events by randomly choosing the emission stage i, the stage decay time t_i, and the energy and momentum (assuming isotropic emission) of each particle according to the input parameters P_i, τ_i, V_i, and T_i. Each particle's emission time is taken as the sum of the decay time of the emission stage plus randomly chosen decay times for the $i-1$ previous stages. The particles' trajectories are calculated numerically, including Coulomb interactions between the coincident particles and between the particles and the residual compound nucleus. Final trajectories of the particles are compared with detector positions to determine which events are "detected." Correlation functions are constructed by generating an event-mixed data set from the simulated events and taking the ratio of the relative-momentum spectra according to Eq. (1). For the simulations presented here, the detector positions and solid angles were taken from the experimental setup. Other experimental constraints such as the low-energy detector thresholds and the energy-dependent neutron detector efficiencies (calculated using the program TOTEFF [42,43]) were also incorporated into the simulations. Consequently, the calculated correlation functions can be directly compared with the data without prior normalization.

The statistical emission parameters P_i, τ_i, V_i, and T_i were chosen in the following fashion. First, a Monte Carlo version of the statistical model code CASCADE [44] was run to simulate the decay of the ^{43}Sc compound system by neutron, proton, deuteron, and alpha-particle emission. For the *np* simulation case, events which contained at least one neutron and proton were further analyzed by forming neutron and proton energy and emission-time distributions as a function of the particle's position in the decay chain. Each event was weighted by a factor representing the number of *np* pairs in the decay chain. For example, the neutron parameters from a *npp* decay chain were weighted twice as much as those from a *np*α decay chain. The parameters P_i, τ_i, V_i, and T_i were then determined from the number of particles emitted and from the calculated energy and time distributions. The parameters for the *pp* case were determined in a similar fashion from events containing at least two protons. The original energy distribution parameters for both the *np* and *pp* cases were optimized to reproduce better our experimental results after comparisons were made between the measured large-opening-angle relative-momentum and laboratory energy spectra and the corresponding spectra calculated by MENEKA. The large-opening-angle data were used for these comparisons because they were found to be relatively free of two-particle correlations which might complicate the comparisons. The optimization significantly reduced the Coulomb barrier parameters for the proton emission, slightly increased the proton emission temperatures, and slightly decreased the neutron emission temperatures. The reduction in the proton Coulomb barrier results because MENEKA includes the Coulomb repulsion between the emitted proton and the compound system during the numerical calculation of the proton trajectory. Consequently, the emission energy on the surface of the compound nucleus will not reflect this energy. It should be pointed out that this method is only a semiempirical parametrization of the particle emission from this reaction. While this is adequate for the present study, more complete measurements would be needed to characterize fully the particle emission from the compound system.

Figure 6 shows comparisons of the 215-MeV ^{16}O+^{27}Al *np* and *pp* correlation data and the correlation functions calculated using MENEKA. The solid curve in the *np* plot corresponds to a MENEKA calculation as described above. The correlation function is flat in this calculation because of the absence of Coulomb repulsion in the *np* system. To account for the d^* peak in the data, a component of simulated singlet deuterons was included in the MENEKA calculations in addition to the independently emitted *np* pairs. The composite d^* particles were emitted isotropi-

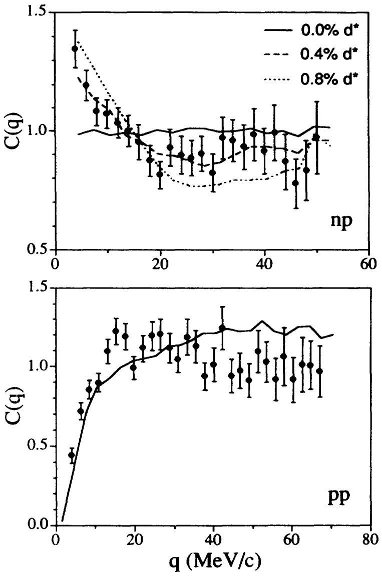

FIG. 6. *np* and *pp* small-angle correlation data compared with correlation functions calculated using the code MENEKA. The three calculations for the *np* case correspond to different mixtures of independently emitted *np* pairs and model d^* particles. The sawtooth nature of the calculated correlation functions results from the statistical uncertainties in the Monte Carlo calculations.

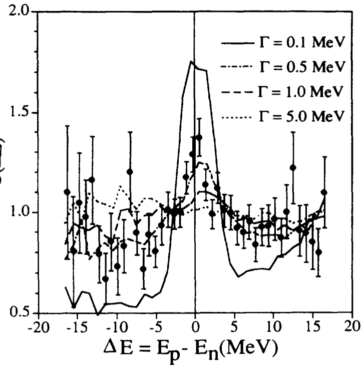

FIG. 7. *np* small-angle correlation data as a function of relative (laboratory) proton-neutron energy compared with MENEKA calculations in which the model d^* state energy width is modified. These calculations used a d^* mixture of 0.4%. A solid vertical line is drawn to indicate zero relative energy.

cally with energy distribution parameters given by $V=2$ MeV, $T=4$ MeV. Once emitted, the d^* particles were accelerated away from the compound nucleus (CN) because of the Coulomb field and then decayed (isotropically) in flight with an exponential lifetime distribution and a Gaussian breakup energy distribution corresponding to a decay energy of 0.07 MeV and a width of 0.5 MeV [4]. While the singlet deuteron does not have a well-defined lifetime because of the virtual nature of the state, for simplicity we made use of an exponential lifetime approximation. Bernstein and Friedman [38] report little difference between similar calculations made using this approximation or the exact decay distribution. The two dashed lines in the *np* plot of Fig. 6 show the correlation functions resulting from a mixture of 0.4% and 0.8% singlet-deuteron emission relative to the independent *np* emission. The effect of the d^* emission is to produce a strong positive correlation in the calculation at small q. The calculation with 0.4% d^* emission produces an excellent fit to the *np* data.

Figure 7 demonstrates the sensitivity of the calculated correlation function to the width of the d^* state. In this case the *np* correlation data are shown as a function of relative (laboratory) energy $\Delta E = E_p - E_n$ and the curves show MENEKA calculations made with a 0.4% d^* contribution for various values of the d^*-state energy width. The vertical line in the plot marks the $E_p = E_n$ point on the energy axis. Two effects are seen in the calculations. First, the width of the observed correlation peak increases with increasing d^* width because of the greater range of relative energy between the two particles. Second, there is a very slight shift in the position of the peak of the correlation function toward larger ΔE for shorter lifetimes (partially obscured by the broader peak widths). This three-body effect results from the differential acceleration of the neutron and proton in the Coulomb field of the residual compound system after the decay of the d^* state. Bernstein and Friedman made a similar calculation of this effect in Ref. [38] and suggested that the shift in the peak position might be used to measure the d^* decay rate without resorting to the $\Gamma = \hbar/\tau$ relationship. Unfortunately, the statistical uncertainty in our data is too large to accurately distinguish between values of Γ in this range. However, the data are consistent with the value $\Gamma = 0.5$ MeV taken from Ref. [4].

The *pp* MENEKA calculation shown in Fig. 6 included only independently emitted proton pairs. One notes general agreement between the trend of the data and the calculation, although the value of the correlation function at $q \geq 40$ MeV/c is overestimated. Two observations are noteworthy. First, the anticorrelation at low q is reproduced by MENEKA without the inclusion of Pauli exclusion effects between the two protons. It may be that, in this reaction, the protons are far enough apart on average (as a result of the time between particle emissions) to subordinate the effect of the Pauli anticorrelation relative to the Coulomb anticorrelation. Second, the slight enhancement of the correlation data in the range $10 \leq q \leq 30$ MeV/c relative to the ratio at larger values of q is not reproduced by the calculation. This peak, as mentioned above, may the result of ^{2}He emission from the CN. In higher-energy reactions, a definite peak is seen in the *pp* correlation function in this region of relative momentum [35]. However, our attempts at calculating the correlation function including a ^{2}He contribution into MENEKA on the level of 0.5% (using a breakup energy of 0.8 MeV and an energy width of 2.8 MeV [4]) did not improve the fit. In fact, the correlation function remained essentially unchanged because of the large enough width of the ^{2}He state which diluted the effect of the ^{2}He correlation. It should be pointed out that the present *pp* analysis is in good agreement with a similar analysis of *pp* correlation data from the ^{16}O+^{27}Al reaction in Ref. [33].

Figure 8 compares the *np* and *pp* correlation data with three Koonin model calculations. The source parametrization in these calculations was taken as a four-dimensional Gaussian with three spatial dimensions of size 4.5 fm (one standard deviation), the approximate radius of the ^{43}Sc compound nucleus. The source extension in time was treated as a parameter τ. The model calculations, which depend upon the product of the *np* or *pp* center-of-mass velocity v and the parameter τ rather than the magnitude of τ alone [3], correspond to three values of $v\tau$ chosen to fit the *np* data. The *pp* calculation included all of the *s* and *p*-wave components of the nuclear force, the Coulomb interaction between the protons, and the identical-fermion antisymmetrization, while the *np* calculation included the dominant *s*-wave nuclear interaction. In both cases the calculations were averaged over the angle between the center-of-mass velocity vector and the relative momentum vector [3] and the curves were normalized to the data in the range $q \geq 35$ MeV/c to account for the normalization shift in the data due to event mixing. One sees that the *np* data are well reproduced for a source with $v\tau \approx 40$ fm. Taking an average *np* velocity on the order of 0.2c, this corresponds to a time difference between *np* emissions of $\tau \approx 7\times10^{-22}$ s, which is on the order of emission times predicted by CASCADE [44] for neutrons and protons from the ^{43}Sc compound system. The *pp* correlation function is not fit as well as the *np* data; the calculation underestimates the correlation function for $q \leq 40$ MeV/c. There is also no evidence in the calculation for the peak in the range $10 \leq q \leq 30$ MeV/c for source sizes consistent with the *np* results. However, the *pp* fit is no worse than that obtained with the MENEKA calculation.

In summary, both the semiclassical evaporation model and the Koonin model describe the *np* correlation data well. However, the source of *np* correlation in the two models (the emission of singlet deuterons in MENEKA and the singlet *s*-wave interaction in the Koonin model) is treated very differently. The *pp* correlation function is not reproduced as well as the *np* data. In the case of the Monte Carlo model, the fit might be improved by the addition of ^{2}He particles into the calculation [35], although our initial attempts along this line were unsuccessful. On the other hand, the *pp* Koonin model result might benefit from using non-Gaussian source distributions [6]. More detailed measurements, including possibly a simultaneous measurement of the *nn* correlation function in addition to the *np* and *pp* systems, are needed to fully test these models.

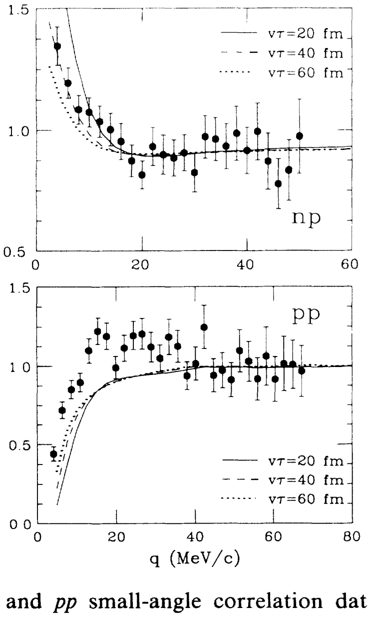

FIG. 8. *np* and *pp* small-angle correlation data compared with correlation functions calculated with the Koonin model. The different calculations correspond to different source sizes.

V. UNSTABLE-STATE YIELDS

The emission yields of several particle-unstable species can be determined from the 215-MeV ^{16}O+^{27}Al coincidence data. The measured yields of singlet deuterons and ^{5}He nuclei as a function of q are given by

$$Y_m(q) = A(q) - \eta B(q) , \tag{4}$$

where $A(q)$ and $B(q)$ are the measured and event-mixed relative-momentum spectra for the *np* or $n\alpha$ coincidence data and η is the background normalization constant for *np* (0.90±0.03) or $n\alpha$ (0.82±0.03) data, which was described in Sec. III. In the application of Eq. (4), one assumes that the correlation function measured in the absence of the d^* or ^{5}He states (but including all other sources of two-particle correlations) would have been flat. This assumption is supported by the *np* MENEKA calculation (with 0.0% d^* mixture) presented in Fig. 6.

The measured yields of ^{6}Li* and ^{5}Li are more difficult to extract from the $d\alpha$ and $p\alpha$ coincidence data because of the presence of Coulomb anticorrelation in these data. For these cases we estimated correlation functions $C'(q)$ that would have been observed in the absence of the ^{6}Li* or ^{5}Li resonances by considering the correlation data on either side of the resonance peaks. These background correlation functions are shown as solid lines in Fig. 9. For the ^{5}Li background, two dashed curves representing upper and lower limits are also shown. The relative-momentum spectrum $A'(q)$ that would have been measured in the absence of either resonance follows from Eq. (1):

$$A'(q) = C'(q)B(q) , \tag{5}$$

leading to a resonance yield given by

$$Y_m(q) = A(q) - A'(q) , \tag{6}$$

where $A(q)$ and $B(q)$ are the measured and event-mixed relative-momentum spectra for the $d\alpha$ or $p\alpha$ coincidence data.

All of the composite-particle yields $Y_m(q)$ depend strongly on the coincident particle detection efficiency of the experimental apparatus, which in turn depends upon properties of the particle detectors (positions, solid angles, energy thresholds, and energy-dependent detection

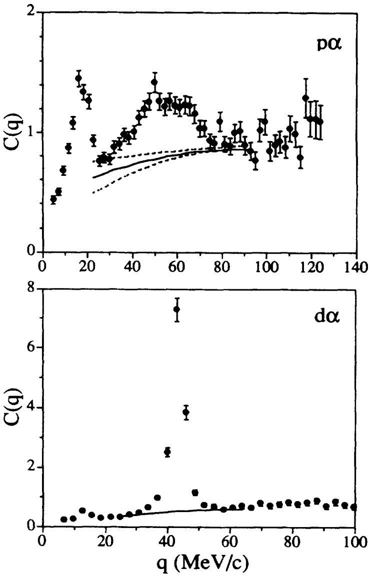

FIG. 9. *pα* and *dα* small-angle correlation data, shown with the backgrounds used in the yield calculations (solid lines). The dashed lines in the *pα* plot show estimates of the background uncertainty.

efficiencies) and upon properties of the composite particle (the emission and breakup energies). We modeled this efficiency using a Monte Carlo event simulation similar to MENEKA to determine the two-particle detection probability as a function of the breakup momentum q of the composite particle. The code simulated the isotropic emission of composite particles from the surface of a ^{43}Sc compound nucleus. The calculation for the d^* detection efficiency used a c.m. emission distribution which corresponded to the measured (ground-state) deuteron energy spectrum, while the ^{5}He calculation used a distribution which corresponded to the measured alpha-particle spectrum. No experimental energy spectra were available for the ^{5}Li and ^{6}Li* cases, and so approximate spectra were derived from the alpha-particle data. First, the alpha-particle laboratory energy spectrum (measured at $\Theta_{\mathrm{lab}}=45°$) was fit with the functional form

$$Y(E)=(E-V_{\mathrm{lab}})^{\gamma}\exp\left[\frac{-E}{T}\right], \tag{7}$$

where V_{lab}, γ, and T were taken as free parameters. The results of the fit gave $V_{\mathrm{lab}}=6.2$ MeV, $\gamma=0.63$, and $T=9.9$ MeV. From this, the c.m. Coulomb barrier for the alpha particles can be calculated ($V_{\mathrm{c.m.}}=4.0$ MeV) and the c.m. Coulomb barrier for $Z=3$ particles can then be estimated by multiplying the alpha-particle barrier by the ratio of the nuclear charges. The result is $V_{\mathrm{c.m.}}=6.0$ MeV, corresponding to laboratory frame barriers of 11.1 and 9.1 MeV, respectively, for the ^{5}Li and ^{6}Li* particles. The ^{5}Li and ^{6}Li* efficiency calculations used c.m. emission distributions corresponding to Eq. (7) with the estimated values for V_{lab} and the alpha-particle values for γ and T. The composite particles, once evaporated, were allowed to decay and the daughter particles' trajectories were calculated in the laboratory frame and compared with the detector positions used in the experiment. All composite-particle decays were assumed to be isotropic in the parent center of mass. The detector thresholds and efficiencies (for neutron detectors) were included as in the MENEKA calculations described previously. The number of coincident particles "detected" from composite-particle breakup was compared with the number emitted (into a solid angle of 4π sr) to define an effective solid angle of the detector assembly:

$$\frac{\Delta\Omega(q)}{4\pi}=\frac{\text{number detected}}{\text{number emitted}}. \tag{8}$$

The composite-particle cross section is then given by

$$\frac{d^2\sigma}{dq\,d\Omega}=\frac{Y_m(q)}{(I_0 n_0 t)\Delta\Omega(q)\Delta q}, \tag{9}$$

where I_0 is the incident ^{16}O beam intensity, $n_0 t$ is the areal density of the target, $Y_m(q)$ is the measured composite-particle yield, and Δq is the bin size in relative momentum in which $Y_m(q)$ was defined. Figures 10 and 11 show the emission cross sections as a function of relative momentum for the composite-particle species considered here. The error bars on the experimental data reflect the statistical uncertainties, the previously quoted errors of η for the d^* and ^{5}He cases, a ±10% estimated error in $C'(q)$ for the ^{6}Li* case, and a background error taken as either the difference between the extremes in $C'(q)$ (for the ^{5}Li case) or ±10% of $C'(q)$, whichever was greater. The curves shown in Figs. 10 and 11 are theoretical relative-momentum distributions taken from Bernstein, Friedman, and Lynch [4] and normalized to the

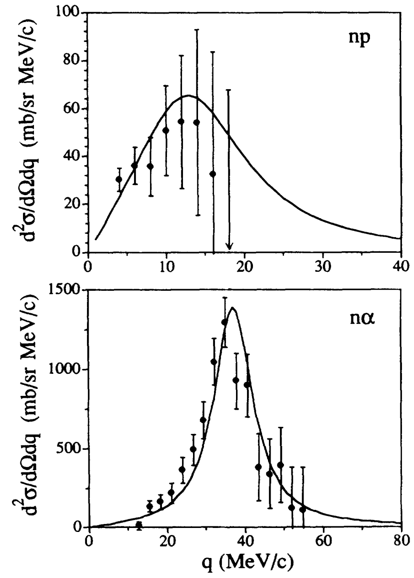

FIG. 10. Emission spectra for singlet deuterons (*np*) and ground-state ^{5}He (*nα*) nuclei shown as a function of relative momentum. The solid lines correspond to the theoretical distributions of Bernstein, Friedman, and Lynch [4], normalized to the data.

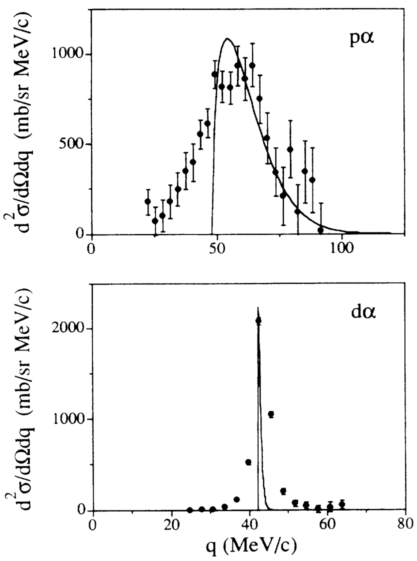

FIG. 11. Emission spectra for ground-state ^{5}Li ($p\alpha$) and 2.186-MeV ^{6}Li* ($d\alpha$) shown as a function of relative momentum. The solid lines correspond to the theoretical distributions of Bernstein, Friedman, and Lynch [4], normalized to the data.

data. The theoretical curves fit the d^* and ^{5}He spectra quite well, although the singlet-deuteron data have large experimental uncertainties. The width of the theoretical ^{6}Li resonance is considerably less than that of the experimental data, from which we deduce that our relative-momentum resolution is 6 MeV/c (FWHM). The ^{5}Li data are fitted reasonably well at high q, but the curve falls more quickly to zero than the data at small q. This discrepancy between the data and curve probably results from the sharp cutoff approximation used for the Coulomb penetrability in the theoretical $p\alpha$ distribution [4].

The total d^* and ^{5}He cross sections were determined by integrating the normalized distributions (solid curves) in Fig. 10. The ^{5}Li and ^{6}Li cross sections were determined by summing the experimental data in Fig. 11 since the theoretical distributions did not reproduce the data very well. The cross sections are listed in Table I, together with the estimated errors due to counting statistics and the background uncertainties. The quoted ^{5}Li and ^{6}Li* errors do not reflect additional uncertainties due to the estimated energy distributions which were used in the efficiency calculations. Modifying the V_{lab}, γ, and T parameters by ±25% (individually) for the ^{5}Li case and recalculating the $p\alpha$ coincidence detection efficiency results in ^{5}Li cross sections between 24.9 and 34.5 mb/sr. Similarly, modifying the ^{6}Li* parameters by ±25% results in cross sections between 10.6 and 15.4 mb/sr.

TABLE I. Emission cross sections for unstable states.

Unstable state	Cross section (mb/sr)
d^*	1.3±0.5
^{5}He	23.8±2.3
^{5}Li	28.5±1.4
^{6}Li*	12.4±1.0

VI. DEUTERON THERMOMETER

The population distribution of states of a composite particle emitted from a thermalized source is given in the thermal model by

$$\frac{dn(E)}{dE}=N\rho(E)\exp\left[\frac{-E}{T}\right], \tag{10}$$

where E is the excitation energy of the fragment, $\rho(E)$ is the density of states, T is the source temperature, and N is a normalization constant [18,23]. For a particle with two particle-unstable resonances well separated in energy, the density of states can be written [18,23]

$$\rho(E)=\frac{2J_1+1}{\pi}\frac{d\eta_1}{dE}+\frac{2J_2+1}{\pi}\frac{d\eta_2}{dE}, \tag{11}$$

where J_1 and J_2 are the spins of the two states and η_1 and η_2 are the energy-dependent scattering phase shifts for the daughter particles of each resonance. The population of each state can be determined as a function of temperature by integrating $dn(E)/dE$ over the respective energy ranges corresponding to the two states. The ratio of emission yields for the two resonances R is then given by the well-known result

$$R=\frac{2J_1+1}{2J_2+1}\exp\left[\frac{-\Delta E}{T}\right], \tag{12}$$

where ΔE is the energy difference between the states. In the case of the deuteron which has only one (unbound) excited state, the density of states becomes

$$\rho(E)=(2J_{\text{g.s.}}+1)\delta(E)+\frac{2J_1+1}{\pi}\frac{d\eta}{dE}, \tag{13}$$

where the first term corresponds to the ground state and the second term represents the ^1S virtual state. The resulting population ratio for singlet- to ground-state deuterons for thermally emitted particles is given by

$$R=\frac{(2J_1+1)}{(2J_{\text{g.s.}}+1)}\int\frac{1}{\pi}\frac{d\eta}{dE}\exp\left[\frac{-E}{T}\right]dE, \tag{14}$$

where the limits of integration are over the excitation energy range of the singlet state. Using limits corresponding to between 0 and 90 MeV/c of relative momentum between the daughter neutron and proton leads to

$$R=\frac{(2J_1+1)}{(2J_{\text{g.s.}}+1)}[F]\exp\left[\frac{-2.26}{T}\right]. \tag{15}$$

This result differs from Eq. (12) only by the constant F, which arises from the integration of the ^{1}S virtual-state phase shifts and depends only weakly upon the value of the temperature T. Using the results of Ref. [45] for the ^1S phase shift, we find that F ranges between 0.33 and 0.34 for T between 0.5 and 5.0 MeV. The upper limit of integration of Eq. (14) was chosen somewhat arbitrarily, but 90 MeV/c is well above the peak in the d^* decay distribution in Fig. 10. Larger or smaller values for the upper limit of integration do not substantially affect the result in Eq. (15).

Equation (15) can be used to determine the source temperature of the $^{16}O+^{27}Al$ reaction zone from the measured d^* and deuteron emission yields. The d^* emission yield is given in Table I. We found the deuteron cross section to be 73±1 mb/sr (at $\Theta_{lab}=45°$) from the deuteron events observed in the NaI(Tl) detectors. These results imply a source temperature of $1.2^{+0.3}_{-0.2}$ MeV. By way of comparison, the first-order Fermi-gas-model temperature of a compound system is given by [46]

$$T=\sqrt{E/a}\ , \tag{16}$$

where E is the excitation energy of the nucleus and $a=A/8$ MeV^{-1} is the level-density parameter (A is the nuclear mass number). This model leads to a temperature estimate of 5.3 MeV, a value similar to the slope temperatures extracted from the coincident neutron and proton energy spectra ($T_n=4.6$ MeV and $T_p=5.0$ MeV, respectively). However, before the d^*/d temperature can be compared with the Fermi-gas-model result, two corrections to the d^*/d ratio must be considered. Both involve enhanced ground-state deuteron production, the first from sequential emission and the second from nonevaporative deuteron emission. Sequential feeding is the process by which one (or both) of the composite-particle states used to compute the temperature is populated not only by direct emission from the compound system, but also through the sequential decay of heavier composite particles (or the same fragment in higher-energy excited states) which were previously emitted from the thermalized source. The yield of composite-particle states arising from sequential emission would not necessarily reflect the source temperature. In the case of the deuteron thermometer, a substantial ground-state deuteron contamination from sequential emission would result in an artificially low nuclear-temperature estimate.

While no other excited states of the deuteron exist to be a source of feeding, contamination from heavier fragments is possible. We made use of a simplified statistical model program [15] to estimate the magnitude of this component of sequential feeding. A brief description of the program is given here. The compound system is assumed to emit a primary distribution of particles with mass and charge (A,Z) according to the formula

$$P(A,Z)\propto(2J+1)\exp\left[\frac{-V_C}{T}+\frac{Q}{T}\right]\ , \tag{17}$$

where J is the spin of the emitted particle, V_C is the Coulomb barrier, Q is the Q-value energy for fragment emission, and T is an adjustable constant—the "effective sequential emission temperature." All fragments with $Z\le 13$ (about one-half the Z of the compound system) were included in the primary distribution, and fragments were emitted in both their ground and known excited states (up to 20 MeV excitation energy [47]). In the case of an excited state, the Q value in Eq. (17) reflects the additional excitation energy of the fragment. The excited states of all of the primary fragments were next allowed to decay via light-particle emission (n, p, d, t, ^3He, α, $2n$ and $2p$) to states of still lighter fragments. The decay of a particular state was determined from its experimental branching ratio, if known, or by a modified Hauser-Feshbach formula (see Ref. [15]). A final population distribution of all fragments was determined after all primary fragments had reached stable states. The difference between the initial and final populations of a given fragment was taken as the sequential feeding contamination. Our interest was in determining the sequential emission contamination in the deuteron cross section, so that the d^*/d ratio could be corrected and a revised temperature calculated. The one free parameter of the sequential emission calculation, T in Eq. (17) above, was varied between 2.0 and 5.0 MeV in order to compare the results with the available data. For $T\le 2$ MeV, the calculated deuteron contamination was negligible. The $T=5.0$ MeV upper limit was chosen based upon results from much higher-energy reactions for which sequential emission calculations were carried out with this model [15,48]. In those cases, values of the sequential emission temperature were found to be on the order of 3–5 MeV. Furthermore, a $T=5$ MeV value is consistent with the initial compound system temperature based upon the Fermi-gas model. Figure 12 shows a comparison between the $A\ge 6$ mass distribution measured by Gilfoyle *et al.* [49] for the 215-MeV $^{16}O+^{27}Al$ reaction at $\Theta_{lab}=25°$ and the final mass distribution predicted by the sequential emission calculation for $T=4$ MeV (arbitrarily normalized). The peak in the data for $A\ge 20$ is due to heavy fusion residues which are not included in the sequential emission mass distribution. For $A<20$, the shapes of the two spectra are qualitatively similar although differing in the production probability for specific mass nuclei. For example, the calculation predicts the yield ratio of $A=9$ to 10 nuclei to be larger than indicated by the data. The top two plots in Fig. 13 show the calculated ratios for ^5Li to $^6Li^*$ (2.186-MeV state) and ^5He to ^5Li yields for several values of the nuclear temperature parameter T (solid circles). For comparison, the ratios determined from the

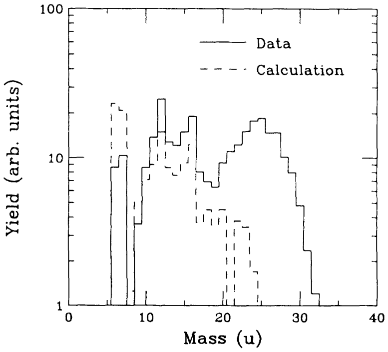

FIG. 12. Comparison of the heavy residue yield measured for the 215-MeV $^{16}O+^{27}Al$ reaction at $\Theta_{lab}=25°$ by Gilfoyle *et al.* [49] with the yield predicted by the sequential emission calculation. The two spectra have been arbitrarily normalized.

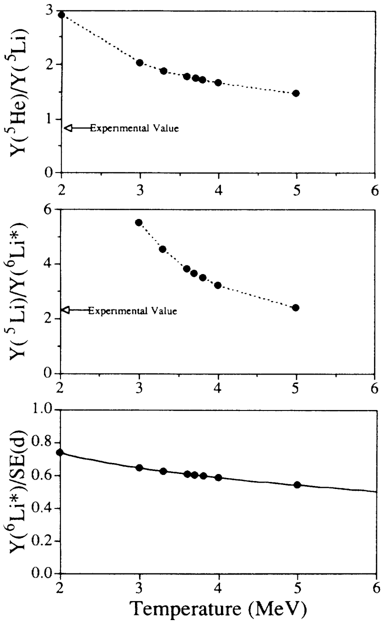

FIG. 13. Upper two plots show the calculated ratio of the ^{5}He (ground state) to ^{5}Li (ground state) and the ^{5}Li (ground state) to ^{5}Li* (2.186-MeV state) yields plotted for several values of the temperature in the sequential emission model (solid circles). The dashed lines in these plots are to guide the eye. The measured value of these ratios, based upon the present work, is indicated in each plot. The bottom plot shows the ratio of the ^{6}Li* (2.186-MeV state) yield to the ground-state deuteron sequential emission yield plotted versus temperature as calculated in the sequential emission model. The solid line in this plot shows the theoretical ratio assuming that all deuteron sequential emission results from ^{6}Li states populated according to the thermal model.

yields measured in this work are also indicated on the plots. In the upper plot, the measured ^{5}He/^{5}Li ratio is found to be considerably smaller than the calculated values, while the center plot shows agreement between the calculated and measured ^{5}Li/^{6}Li* ratio for $T \approx 5$ MeV. These discrepancies probably indicate that the initial population assumption given in Eq. (17) is too simplified to explain this level of detail. Possibly a more complete statistical model description of the ^{43}Sc decay, including all of the compound system decay channels, would better predict the production probabilities of individual nuclei. However, one important conclusion of the present calculations is that sequential deuteron emission results almost entirely from the decay of ^{6}Li, the only $A < 10$ nucleus with low-lying excited states that decay predominantly by deuteron emission. This is illustrated in the bottom plot of Fig. 13, where the calculated ratio of the population of ^{6}Li* (2.186-MeV state) to the deuteron sequential emission yield is plotted as a function of the nuclear temperature parameter T (solid circles). The solid line represents the theoretical ratio when all of the deuteron sequential emission yield results from excited ^{6}Li states. This latter curve was generated using the deuteron branching ratios of Ref. [50] for the ^{6}Li states and assuming an initial population distribution of the excited ^{6}Li states relative to the ground state given by Eq. (12). Based upon the value of this ratio for $T \leq 5$ MeV (corresponding to a value for the ratio ≥ 0.54) and the measured ^{6}Li* (2.186-MeV state) yield of 12.4 mb/sr, we deduce a possible deuteron sequential emission contamination of 23 mb/sr in our 73-mb/sr deuteron yield. A lower source temperature would, of course, lead to a smaller predicted contamination. However, the measured ^{6}Li* yield (12.4 mb/sr) provides a lower limit to the deuteron sequential emission yield.

A second source of ground-state deuteron contamination is noncompound emission. These are particles produced not by fusion evaporation, but rather in more peripheral reactions where the deuteron emission cannot be quantified in terms of evaporation from a thermalized source. If these "direct" deuterons are preferentially emitted in the ground state, the d^*/d ratio will be underestimated. We determined this component of the deuteron cross section by examining the angular dependence of the experimental deuteron emission spectra. Figure 14 shows the deuteron yield measured by Gordon *et al.* [51] for the ^{16}O+^{27}Al reaction at $E(^{16}\text{O})=215$ MeV, plotted as a function of c.m. emission angle for five c.m. energy bins. Deuterons evaporated from a compound nucleus will have angular distributions which are symmetric about $\Theta_{\text{c.m.}}=90°$. The data show evidence for enhanced yield at forward angles, characteristic of noncompound-particle emission, especially in the high-energy bins. The percentage of noncompound yield in each energy bin was determined by comparing the deuteron emission at the (energy-bin-dependent) c.m. angle corresponding to the laboratory angle of 45° with the yield at the symmetric angle $\Theta_{\text{c.m.}} > 90°$. The difference

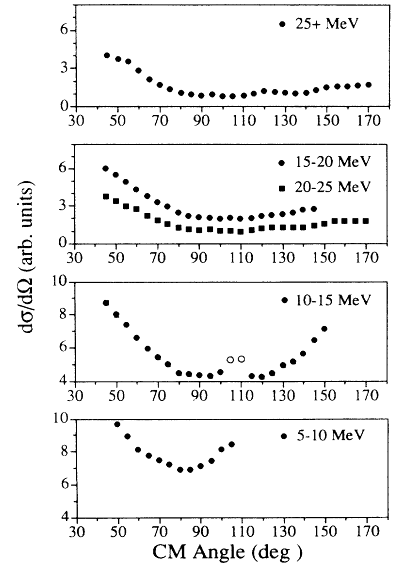

FIG. 14. Ground-state deuteron angular distributions for the 215-MeV ^{16}O+^{27}Al reaction measured by Gordon *et al.* [51], plotted for five deuteron c.m. energy ranges. The statistical uncertainties are the same size or smaller than the plotted points. The two open circles in the 10–15-MeV plot are discussed in the text.

in the two yields relative to the yield in the forward direction was taken as the percentage of noncompound emission. The values were 0% for the 5–10-MeV bin, 13% for the 10–15-MeV bin, 49% for the 15–20-MeV bin, 60% for the 20–25-MeV bin, and 57% for the (25+)-MeV bin. The lowest energy deuterons (below 5 MeV; not illustrated) were all assumed to be due to compound emission. These values were then multiplied by the portion of the measured 73 mb/sr of deuteron cross section in each energy bin (23.9, 16.2, 9.3, 4.9, and 3.9 mb/sr for the 5–10-, 10–15-, 15–20-, 20–25-, and (25+)-MeV energy bins, respectively) to yield a noncompound deuteron cross section of 12 mb/sr. Discounting of the two anomalously high data points at $\Theta_{\mathrm{c.m.}}=105°$ and 110° in the 10–15-MeV angular distribution (plotted as open circles in Fig. 14) results in a 14-mb/sr cross section. Combining the 14-mb/sr result with the estimated sequential emission cross section (23 mb/sr), we estimate a revised d^*/d ratio of 0.036 ± 0.014, leading to a source temperature of $T=2.0^{+0.8}_{-0.6}$ MeV. The quoted uncertainties result from the uncertainties in the d^* and d cross sections. For comparison, using the lower limit on the sequential emission cross section (12.4 mb/sr) leads to $T=1.6^{+0.5}_{-0.4}$ MeV.

It is this corrected d^*/d temperature that is properly compared with a Fermi-gas-model estimate. However, the first-order temperature estimate given by Eq. (16) does not account for the cooling of the compound system during particle emission or for the excitation energy bound up in collective motion. A better temperature estimate was calculated within the statistical model by averaging over the deuteron emission process. First, a Monte Carlo version of the evaporation code CASCADE [44] was used to simulate the decay of 5×10^4 ^{43}Sc compound nuclei by the evaporation of neutrons, protons, deuterons, and alpha particles. The average excitation energy, mass, and spin of the residual compound nuclei was computed as a function of the number of particles emitted (the decay stage). These averages are listed in Table II, along with the number of deuterons evaporated in each decay stage. The average nuclear temperature was calculated for each decay stage according to the expression

$$T=\sqrt{(E^*-E_{\mathrm{rot}})/a}\ , \tag{18}$$

where a is the level-density parameter, as before, and E_{rot} is the excitation energy bound up in collective (rotational) motion of the compound system. The rotational energy was calculated from the formula

$$E_{\mathrm{rot}}=\frac{\hbar^2 I(I+1)}{2\Theta}\ , \tag{19}$$

where I is the average nuclear spin and Θ is the nuclear moment of inertia, taken to be 85% of the spherical rigid-body moment of inertia using a radius parameter of $r_0=1.4$ fm. The average rotational energy and temperature at each stage are also listed in Table II. The nuclear temperature to be compared with the d^*/d result was obtained by calculating the number of d^* emitted in each stage from the temperature T and number of deuterons emitted in the stage (according to the thermal model [Eq. (15)]) and using the total number of deuterons and d^* emitted to calculate the average d^*/d temperature from Eq. (15). The temperature which results from this averaging procedure is 4.3 MeV, still considerably higher than the maximum corrected d^*/d temperature of $T=2.0^{+0.8}_{-0.6}$ MeV. In fact, one would have to account for an additional 16 mb/sr of deuteron cross section due to "direct" or sequential emission to achieve a d^*/d temperature of 4.3 MeV. It should be noted that this result is unchanged if one considers incomplete fusion rather than complete fusion for the $^{16}\mathrm{O}+^{27}\mathrm{Al}$ reaction. For the fusion of beam velocity ^{12}C with ^{27}Al, the average d^*/d temperature estimated by the above procedure is 4.4 MeV.

In light of the low d^*/d temperature observed in the $^{16}\mathrm{O}+^{27}\mathrm{Al}$ reaction, it is easier to understand why no singlet-deuteron correlation was observed in the lower-energy $^{16}\mathrm{O}+^{12}\mathrm{C}$ reaction. In this situation the reaction energy was low enough that little deuteron contamination is expected from either sequential emission or noncompound reaction mechanisms. Figure 3 shows the experimental np correlation data compared with calculated correlation functions for source temperatures of 1.0, 1.5, and 2.0 MeV. The theoretical correlation functions were

TABLE II. Summary of the average properties of residual compound nuclei during the evaporative decay process of the ^{43}Sc compound nucleus.

Decay stage	E^* (MeV)	Average A	Spin	E^{rot} (MeV)	T (MeV)	Number of deuterons emitted[a]
0	149	43.0	22.7	21.2	4.9	11 841
1	127	41.3	20.8	19.2	4.6	11 873
2	106	39.5	18.4	16.2	4.3	11 047
3	85.6	37.7	16.1	13.5	3.9	8356
4	66.4	35.8	13.8	11.0	3.5	4507
5	48.6	33.8	11.4	8.3	3.1	1651
6	31.8	31.8	9.0	5.8	2.6	461
7	16.9	29.9	6.7	3.7	1.9	62
8	8.1	28.9	5.1	2.4	0.9	0

[a] Per 50 000 decays.

formed by taking the ratio of the event-mixed relative-momentum spectrum, after adding a calculated contribution due to d^* events, to the original event-mixed spectrum (renormalized to have the same total number of events as the original data plus the extra d^* events). The d^* contribution was calculated relative to the measured ground-state deuteron cross section of 7 mb/sr at $\Theta_{\mathrm{lab}}=15°$, assuming d^* emission according to the thermal model [Eq. (15)], with a breakup distribution according to Bernstein, Friedman, and Lynch [4] (shown in Fig. 10), and using the coincident neutron-proton detection efficiency calculated for this experimental setup using the technique described for the $^{16}\mathrm{O}+{}^{27}\mathrm{Al}$ setup. For orientation, the $^{28}\mathrm{Si}$ compound-nucleus temperature is estimated to be 3.0 MeV in the first-order Fermi-gas model and 2.9 MeV if the temperature is averaged over the d^* emission process as was done for the $^{16}\mathrm{O}+{}^{27}\mathrm{Al}$ reaction. The slope temperature for neutrons measured in coincidence with protons in this experiment was 1.8 MeV. From Figure 3, one sees that the correlation data are consistent with a source temperature less than 1 MeV, again well below the Fermi-gas-model estimate for the nuclear temperature.

The tendency to measure low source temperatures via the population-ratio technique (as compared with the slope temperature, for example) is well documented for a variety of different composite particles and over a wide range of reaction energies [11–21, 23]. Sometimes, but not always, it is possible to reconcile the nuclear and Fermi-gas-model temperatures due to the uncertainties in the sequential feeding, other nonthermal sources of particles, or in the experimental data. Attempts to explain the discrepancies have focused on the emission dynamics of the composite particles and the possibility that non-Boltzmann temperature distributions of excited states are produced under certain conditions [52–55]. We have found a similar temperature discrepancy in the $^{16}\mathrm{O}+{}^{27}\mathrm{Al}$ reaction at 215 MeV bombarding energy and the $^{16}\mathrm{O}+{}^{12}\mathrm{C}$ reaction at 60.5 MeV bombarding energy, when probed via the deuteron thermometer. It appears in these cases that either the source temperatures that are relevant for deuteron emission are well below the Fermi-gas-model estimates or that the d^* emission is suppressed relative to the thermal model prediction.

VII. CONCLUSION

We have reported on neutron-proton, neutron-deuteron, and neutron–alpha-particle small-angle correlation data from the 215-MeV $^{16}\mathrm{O}+{}^{27}\mathrm{Al}$ reaction and neutron-proton correlation data from the 60.5-MeV $^{16}\mathrm{O}+{}^{12}\mathrm{C}$ reaction. These data provide the first measurement of neutron–light-charged-particle correlation functions. In addition, the proton-proton correlation function, as well as several other LCP-LCP correlation functions, were simultaneously measured for the $^{16}\mathrm{O}+{}^{27}\mathrm{Al}$ reaction. The $^{16}\mathrm{O}+{}^{27}\mathrm{Al}$ np and $n\alpha$ correlation data showed strong positive correlations corresponding to singlet-deuteron and $^{5}\mathrm{He}$ production. Positive correlations due to ground-state $^{5}\mathrm{Li}$ and 2.186-MeV-state $^{6}\mathrm{Li}$ were seen in the $p\alpha$ and $d\alpha$ coincidence data, respectively. An interesting anticorrelation was observed in the nd correlation function at low relative momentum, possibly the result of coalescence of low-q nd pairs or a repulsive component of the nd nuclear force.

The np correlation function for the $^{16}\mathrm{O}+{}^{27}\mathrm{Al}$ reaction was successfully modeled with both the Koonin model, from which a "source lifetime of $v\tau=40$ fm was obtained," or by means of a semiclassical Monte Carlo evaporation model. This latter model includes the emission of independently emitted neutrons and protons as well as composite singlet deuterons which decay into highly correlated np pairs. With this model, one determines the ratio of singlet deuterons emitted relative to independently emitted np pairs. In our case this ratio was approximately 0.4%. The pp correlation data were not fitted as well by either model, although the Koonin model results might be improved using non-Gaussian source distributions and the evaporation model results by inclusion of $^{2}\mathrm{He}$ particles.

Composite-particle yields for singlet deuterons, the ground state of $^{5}\mathrm{He}$ and $^{5}\mathrm{Li}$, and the 2.186-MeV state of $^{6}\mathrm{Li}$ were determined from the small-angle coincidence data from the $^{16}\mathrm{O}+{}^{27}\mathrm{Al}$ reaction. The relative momentum breakup spectra of these composite particles are in good agreement with the predictions of Bernstein, Friedman, and Lynch [4].

Finally, a nuclear temperature of $T=2.0^{+0.8}_{-0.6}$ MeV is calculated for the $^{16}\mathrm{O}+{}^{27}\mathrm{Al}$ compound system from the ratio of singlet to ground-state deuteron production in the reaction, after corrections for sequential emission and noncompound deuteron production were made. This value is much lower than the 4.4 MeV temperature calculated for the compound system in the Fermi-gas model. Similarly, the d^*/d temperature in the $^{16}\mathrm{O}+{}^{12}\mathrm{C}$ reaction is estimated to be $T<1$ MeV, which is also well below the 2.9 MeV temperature estimated for the $^{28}\mathrm{Si}$ compound system. These results indicate that singlet-deuteron production is strongly suppressed relative to the thermal model prediction for these two rather different systems. The explanation for these low source temperatures measured by the d^*/d thermometer is not known, although several possible models for non-Boltzmann emission distributions have been suggested for composite-particle excited states. These include a rapidly expanding source [54,55], and a source which interacts via the nuclear force with the composite particles in a fashion so that the Boltzmann distribution is no longer valid [53]. The latter model may be especially appropriate for an extended particle such as the deuteron.

This work was supported in part by the National Science Foundation under Grant Nos. PHY91-00688 and PHY89-07170 and by the William and Flora Hewlett Foundation of the Research Corporation.

---

[1] For a recent review, see D. H. Boal, C. K. Gelbke, and B. K. Jennings, Rev. Mod. Phys. **62**, 553 (1990).

[2] G. I. Kopylov and M. I. Podgoretskii, Yad. Fiz. **19**, 434 (1974) [Sov. J. Nucl. Phys. **19**, 215 (1974)].

[3] S. E. Koonin, Phys. Lett. **70B**, 43 (1977).

[4] M. A. Bernstein, W. A. Friedman, and W. G. Lynch, Phys. Rev. C **29**, 132 (1984); **30**, 412(E) (1984).

[5] B. K. Jennings, D. H. Boal, and J. C. Shillcock, Phys. Rev. C **33**, 1303 (1986).

[6] W. G. Gong, W. Bauer, C. K. Gelbke, and S. Pratt, Phys. Rev. C **43**, 781 (1991).

[7] Yu. D. Bayukov, P. V. Degtyarenko, Yu. V. Efremenko, V. B. Fedorov, V. B. Gavrilov, N. A. Goryainov, Yu. G. Grishuk, O. B. Gushchin, I. A. Klumov, G. A. Leksin, A. V. Stavinsky, V. P. Surin, S. M. Shuvalov, and B. B. Shvartsman, Phys. Lett. B **189**, 291 (1987).

[8] W. Dunnweber, W. Lippich, D. Otten, W. Assmann, K. Hartmann, W. Hering, D. Konnerth, and W. Trombik, Phys. Rev. Lett. **65**, 297 (1990).

[9] B. Jakobsson, B. Noren, A. Oskarsson, M. Westenius, M. Cronqvist, S. Mattson, M. Rydehell, O. Skeppstedt, J. C. Godrand, B. Khelfaoui, S. Kox, F. Merchez, C. Perrin, D. Rebreyend, L. Westerberg, and S. Pratt, Phys. Rev. C **44**, R1238 (1991).

[10] S. Pratt, Phys. Rev. C **40**, 168 (1989).

[11] D. J. Morrissey, W. Beneson, E. Kashy, C. Bloch, M. Lowe, R. A. Blue, R. M. Ronningen, B. Sherrill, H. Utsunomiya, and I. Kelson, Phys. Rev. C **32**, 877 (1985).

[12] D. J. Morrissey, C. Bloch, W. Benenson, E. Kashy, R. A. Blue, R. M. Ronningen, and R. Aryaeinejad, Phys. Rev. C **34**, 761 (1986).

[13] A. D'Onofrio, B. Delaunay, H. Dumont, J. Gomez del Campo, A. Brandi, R. Moro, M. Romano, F. Temasi, and J. F. Bruandet, Z. Phys. A **326**, 335 (1987).

[14] J. Gomez del Campo, J. L. Charvet, A. D'Onofrio, R. L. Auble, J. R. Beene, M. L. Halbert, and H. J. Kim, Phys. Rev. Lett. **61**, 290 (1988).

[15] H. M. Xu, W. G. Lynch, C. K. Gelbke, M. B. Tsang, D. J. Fields, M. R. Maier, D. J. Morrissey, T. K. Nayak, J. Pochodzalla, D. G. Sarantites, L. G. Sobotka, M. L. Halbert, and D. C. Hensley, Phys. Rev. C **40**, 186 (1989).

[16] J. Gomez del Campo, R. L. Auble, J. R. Beene, M. L. Halbert, H. J. Kim, A. D'Onofrio, and J. L. Charvet, Phys. Rev. C **43**, 2689 (1991).

[17] J. H. Lee, W. Benenson, C. Bloch, Y. Chen, R. J. Radtke, E. Kashy, M. F. Mohar, D. J. Morrissey, R. Blue, and R. M. Ronningen, Phys. Rev. C **41**, 2406 (1990).

[18] J. Pochodzalla, C. K. Gelbke, W. G. Lynch, M. Maier, D. Ardouin, H. Delagrange, H. Doubre, C. Gregoire, A. Kyanowski, W. Mittig, A. Peghaire, J. Peter, F. Saint-Laurent, B. Zwieglinski, G. Bizard, F. Lefebvres, B. Tamain, J. Quebert, Y. P. Viyogi, W. A. Friedman, and D. H. Boal, Phys. Rev. C **35**, 1695 (1987).

[19] Z. Chen, C. K. Gelbke, W. Gong, Y. D. Kim, W. G. Lynch, M. R. Maier, J. Pochodzalla, M. B. Tsang, F. Saint-Laurent, D. Ardouin, H. Delagrange, H. Doubre, J. Kasagi, A. Kyanowski, A. Peghaire, J. Peter, E. Rosato, G. Bizard, F. Lefebvres, B. Tamain, J. Quebert, and Y. P. Viyogi, Phys. Rev. C **36**, 2297 (1987).

[20] C. K. Gelbke, Nucl. Phys. **A495**, 27c (1989).

[21] F. Saint-Laurent, A. Kyanowski, D. Ardouin, H. Delegrange, H. Doubre, C. Gregoire, W. Mittig, A. Peghaire, J. Peter, G. Bizard, F. Lefebvres, B. Tamain, J. Quebert, Y. P. Viyogi, J. Pochodzalla, C. K. Gelbke, W. Lynch, and M. Maier, Phys. Lett. B **202**, 190 (1988).

[22] R. A. Kryger, J. J. Kolata, W. Chung, S. Dixit, R. J. Tighe, J. J. Vega, P. A. DeYoung, C. Copi, J. Sarafa, D. G. Kovar, G. P. Gilfoyle, and S. K. Sigworth, Phys. Rev. Lett. **65**, 2118 (1990).

[23] T. K. Nayak, T. Murakami, W. G. Lynch, K. Swartz, D. J. Fields, C. K. Gelbke, Y. D. Kim, J. Pochodzalla, M. B. Tsang, H. M. Xu, and F. Zhu, Phys. Rev. C **42**, 132 (1992).

[24] Havar foil is manufactured by the Hamilton Watch Co.

[25] P. A. DeYoung, B. L. McGrath, and W. F. Piel, Jr., Nucl. Instrum. Methods **226**, 555 (1984).

[26] M. S. Gordon, Ph.D. thesis, State University of New York at Stony Brook, 1988.

[27] C. F. Maguire, D. G. Kovar, C. Beck, C. N. Davids, M. F. Vineyard, F. W. Prosser, S. V. Reinert, J. J. Kolata, and K. Kwiatkowski (unpublished). An extensive article on the properties of NaI(Tl) detectors is in progress for submission to Nucl. Instrum. Methods.

[28] J. Heltsky, L. Brandon, A. Galonsky, L. Heilbronn, B. A. Remington, S. Langer, A. Vander Molen, and J. Yurkon, Nucl. Instrum. Methods A **263**, 441 (1988).

[29] W. A. Zajc, J. A. Bistirlich, R. R. Bossingham, H. R. Bowman, C. W. Clawson, K. M. Crowe, K. A. Frankel, J. G. Ingersoll, J. M. Kurck, C. J. Martoff, D. L. Murphy, J. O. Rasmussen, J. P. Sullivan, E. Yoo, O. Hashimoto, M. Koike, W. J. McDonald, J. P. Miller, and P. Truol, Phys. Rev. C **29**, 2173 (1984).

[30] See M. A. Lisa, W. G. Gong, C. K. Gelbke, and W. G. Lynch, Phys. Rev. C **44**, 2865 (1991), and references therein.

[31] S. A. Sofianos, A. Papastylianos, H. Fiedeldey, and E. O. Alt, Phys. Rev. C **42**, R506 (1990).

[32] P. A. DeYoung, M. S. Gordon, Xiu qin Lu, R. L. McGrath, J. M. Alexander, D. M. de Castro Rizzo, and L. C. Vaz, Phys. Rev. C **39**, 128 (1989).

[33] P. A. DeYoung, C.J. Gelderloos, D. Kortering, J. Sarafa, K. Zienert, M. S. Gordon, B. J. Fineman, G. P. Gilfoyle, X. Lu, R. L. McGrath, D. M. de Castro Rizzo, J. M. Alexander, G. Auger, S. Kox, L. C. Vaz, C. Beck, D. J. Henderson, D. G. Kovar, and M. F. Vineyard, Phys. Rev. C **41**, R1885 (1990).

[34] See, for example, Refs. [18] and [19].

[35] M. A. Bernstein, W. A. Friedman, W. G. Lynch, C. B. Chitwood, D. J. Fields, C. K. Gelbke, M. B. Tsang, T. C. Awes, R. L. Ferguson, F. E. Obenshain, F. Plasil, R. L. Robinson, and G. R. Young, Phys. Rev. Lett. **54**, 402 (1985).

[36] J. Pochodzalla, W. A. Friedman, C. K. Gelbke, W. G. Lynch, M. Maier, D. Ardouin, H. Delagrange, H. Doubre, C. Gregoire, A. Kyanowski, W. Mittig, A. Peghaire, J. Peter, F. Saint-Laurent, Y. P. Viyogi, B. Zwieglinski, G. Bizard, F. Lefebvres, B. Tamain, and J. Quebert, Phys. Lett. **161B**, 256 (1985).

[37] J. Pochodzalla, C. K. Gelbke, C. B. Chitwood, D. J. Fields, W. G. Lynch, M. B. Tsang, and W. A. Friedman, Phys. Lett. B **175**, 275 (1986).

[38] M. A. Berstein and W. A. Friedman, Phys. Rev. C **31**, 843 (1985).

[39] A. Elmaani, N. N. Ajitanand, T. Ethvignot, and J. M. Alexander (unpublished). MENEKA is an extension of the code KALLIOPI described in R. L. McGrath, A. Elmaani, J. M. Alexander, P. A. DeYoung, T. Ethvignot, M. S. Gordon, and E. Renshaw, Comput. Phys. Commun. **59**, 507 (1990).

[40] B. Erazmus, N. Carjan, and D. Ardouin, Phys. Rev. C **44**, 2663 (1991).

[41] W. G. Gong, Y. D. Kim, and C. K. Gelbke, Phys. Rev. C **45**, 863 (1992).

[42] R. J. Kurtz, University of California Radiation Laboratory Internal Report No. UCR1-11339, 1964.

[43] R. R. Doering, Ph.D. dissertation, Michigan State University, 1974.

[44] F. Puhlhofer, Nucl. Phys. **A280**, 267 (1977).

[45] H. P. Noyes and H. M. Lipinski, Phys. Rev. C **4**, 995 (1971).

[46] Pierre Marmier and Eric Sheldon, *The Physics of Nuclei and Particles* (Academic, New York, 1969), Vol. II, p. 1234.

[47] Fusion followed by fission, which would lead to highly excited fragments with mass $A \approx 20$, were ignored. CASCADE calculations suggest less than 4% of the compound nuclei from the 215-MeV ^{16}O+^{27}Al reaction decay by fission.

[48] Z. Chen and C. K. Gelbke, Phys. Rev. C **38**, 2630 (1988).

[49] G. P. Gilfoyle, M. S. Gordon, R. L. McGrath, G. Auger, J. M. Alexander, D. G. Kovar, M. F. Vineyard, C. Beck, D. J. Henderson, P. A. DeYoung, and D. Kortering, Phys. Rev. C **46**, 265 (1992).

[50] F. Ajzenberg-Selove, Nucl. Phys. **A490**, 1 (1988).

[51] M. S. Gordon *et al.* (unpublished).

[52] D. H. Boal and J. C. Shillcock, Phys. Rev. C **33**, 549 (1986).

[53] N. R. Dagdeviren, Phys. Lett. B **176**, 283 (1986).

[54] W. A. Friedman, Phys. Rev. Lett. **60**, 2125 (1988).

[55] H. W. Bartz, J. P. Bondorf, J. A. Lopez, and H. Schulz, Phys. Rev. C **37**, 2910 (1988).